Construction and Building Materials 469 (2025) 140385

Contents lists available at ScienceDirect

Construction and Building Materials

journal homepage: www.elsevier.com/locate/conbuildmat

Drying-induced deformation in concrete: Insights from a 5-Year study

Petr Havlásek [a,*], Vít Šmilauer [a], Václav Nežerka [b]

[a] Czech Technical University in Prague, Faculty of Civil Engineering, Department of Mechanics, Thákurova 7, 166 29 Prague 6, Czech Republic
[b] Czech Technical University in Prague, Faculty of Civil Engineering, Department of Physics, Thákurova 7, 166 29 Prague 6, Czech Republic

ARTICLE INFO

Keywords:
Drying shrinkage
Creep
Microcracking
Concrete
Modeling
Cyclic humidity

ABSTRACT

Conventional shrinkage and creep experiments do not effectively distinguish between the individual deformation mechanisms. To overcome this problem, a comprehensive experimental study comprising a set of simply supported plain concrete beams with varying dimensions and sealing configurations has been initiated. The five-year data formed the foundation for improving the model based on the Microprestress-solidification theory, which has been found to overestimate creep under fluctuating humidity conditions. The shrinkage response to nonsymmetric drying suggests that the generally accepted Bažant-Najjar model predicts an incorrect distribution of relative humidity. Furthermore, the findings support the nonlinear dependence of drying shrinkage on relative humidity previously identified at the mesoscale.

1. Introduction

The time-dependent behavior of concrete is strongly affected by the evolution of relative humidity, whose decrease induces shrinkage and accelerates short-term creep [1,2]. Furthermore, relative humidity strongly impacts the moisture transport properties of concrete whose diffusivity in the fully dried state is only about 5% of the value at free saturation with a steep transition around the relative humidity of pores $h \approx 0.75$ [1,3,4]. In natural ambient conditions and even for small laboratory specimens, the drying profile is inherently nonuniform and produces shrinkage strains internally restrained by the cross section, leading to self-equilibrated stresses. On the drying surface, these stresses are initially tensile and can easily reach the tensile strength of the material, thus initiating cracking. The magnitude of the generated tensile stresses depends primarily on the drying rate and the magnitude of the shrinkage, which decreases with increasing maturity. As the internal relative humidity equilibrates with the ambient conditions, the distribution of shrinkage eigenstrain becomes almost uniform over the cross section and stress-free. However, due to inelastic processes that relieve shrinkage-induced stresses (mainly creep and partially irrecoverable microcracking), at the final stage of drying, tensile and compressive stresses are expected to develop in the core and on the drying surface, respectively [1,5–7], yet there is no direct experimental evidence. Together with the age dependence of the shrinkage coefficient [8–10] and material stiffness [2,7,11,12], these strains are responsible for the size-effect on drying shrinkage [13,14].

The creep and shrinkage databases [15,16] are built on experiments whose scope and setup, e.g., [17–22], are tailored for the development of code-like prediction models that use the so-called average cross-sectional approach. The primary objective of such experiments is to determine the time-dependent behavior as a function of the given concrete strength, composition of the concrete mixture, the ambient conditions, and finally, in the case of creep experiment, the age at loading.

For instance, the extended Northwestern University database, currently curated at CTU in Prague [15], incorporates a total of 1737 concrete mixes, 1466 creep datasets, and 3540 shrinkage data sets. However, despite the comprehensive nature of this dataset, only a relatively small number of these data sets (19) include both drying shrinkage and the complementary basic and drying creep experiments on matching specimens. Furthermore, only half of those datasets meet the additional experimental completeness and duration criteria, which are critical for analyzing the interaction between drying shrinkage and drying creep.

Creep and shrinkage databases can provide a sound basis for the development and calibration of models that use so-called average cross-sectional approach typically used in engineering practice. Yet, for the advancement or validation of more sophisticated models that operate on so-called material-point approach, such as those discussed in [23–27], more information not only on the underlying physical mechanisms is required. A typical practice is that such complex models are calibrated on the basis of not fully compatible experimental data coming from various sources.

Furthermore, previous research by the authors indicates that the conventional experimental setup, where the specimen is symmetrically

* Corresponding author.
E-mail addresses: petr.havlasek@cvut.cz (P. Havlásek), vit.smilauer@cvut.cz (V. Šmilauer), vaclav.nezerka@cvut.cz (V. Nežerka).

https://doi.org/10.1016/j.conbuildmat.2025.140385
Received 3 October 2024; Received in revised form 23 December 2024; Accepted 8 February 2025
Available online 21 February 2025

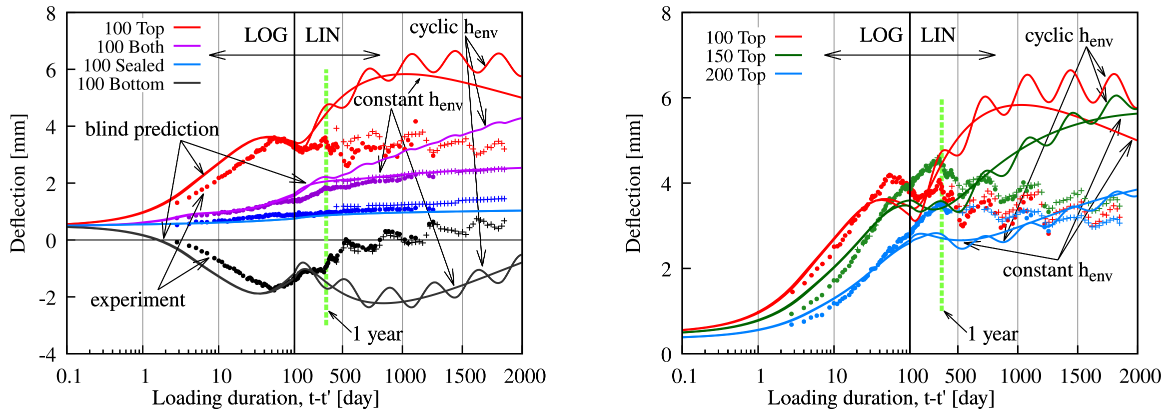

Fig. 1. 5-year evolution of midspan deflection and blind FEM prediction [5] assuming constant ambient humidity (h_{env} = 0.46, solid lines) and cyclic humidity reflecting annual variations in relative humidity (Fig. 3, dashed lines).

exposed to drying without precise knowledge of moisture loss or internal relative humidity distribution, leads to ambiguous determination of material parameters of the constitutive models.

1.1. CTU creep experiment

In 2019, a comprehensive experimental campaign was initiated in CTU in Prague to address the scarcity of reliable experimental data measured on ordinary strength concrete that covers the most common time-dependent phenomena in concrete — drying, shrinkage, creep, and microcracking — and their interaction [5]. Unlike conventional experiments on time-dependent behavior of concrete, the objective of the present experiment is to create an extensive and consistent data set for the development and calibration of advanced material models that operate on the material-point approach, whose behavior is closely related to underlying physical mechanisms, such as moisture transport or concrete hydration.

To achieve that, a more diverse experimental setup is required. In the present study, conventional strength, stiffness, creep, shrinkage, and moisture loss measurements are complemented by the monitoring of partially sealed unreinforced concrete beams loaded by self-weight and subjected to drying. The span and depth of the beams, which represent the core part of the experimental program, range from 1.75 m to 3.0 m and from 0.05 m to 0.20 m, respectively. The dimensions and setup were designed such that the maximum bending stress due to permanent loading was ≈ 1.0 MPa. For the sake of maximum consistency, all specimens were prepared from a single batch of ready-mix concrete.

In conventional creep and shrinkage experiments, only the axial deformation is measured; if the specimen is drying, shrinkage, creep and microcracking interact, but only the overall response is known. Changing the sealing configuration and/or size of the concrete beams allows to generate a much wider variety of responses in which the individual mechanisms interact. This should allow us to identify them more clearly. At the same time, the structural behavior is transparent and allows for a relatively simple instrumentation and efficient computational modeling.

Localized cracking in unreinforced concrete beams can possibly cause misinterpretation of the measured data and lead to seemingly higher compliance. To prevent this, vertical deflection is measured at several different locations along the beams' length. As shown later in Section 2.3, in the present experiment, the measured deflections correspond to the same value of curvature, which indicates that there is no localized crack in the specimen.

Undoubtedly, the data-set can be furthermore enriched by incorporating reinforced [28] or prestressed [29] concrete beams. However, these features would bring other unknowns associated with the mechanical properties of the bond or stress relaxation in steel.

A comprehensive description of the complete experimental setup and comparison of the first-year data with the blind prediction is presented in [5]. A brief overview of the experiment is given in Section 2.1.

1.2. Motivation and objectives

The blind prediction presented in the previous paper [5] which summarized the results within the first year of the experiment, exhibited an extremely good agreement with the measurements.

The prediction was done in open-source finite element solver OOFEM [30,31] using a single-coupled hygromechanical scheme combining moisture transport described by the Bažant and Najjar model for diffusion [3] with the modified MPS model [32,33] for concrete creep and shrinkage extended with fixed-crack model [34] and regularized using the crack-band approach [35]. In the simulation, the ambient conditions (relative humidity h_{env} and temperature) were set to their one-year average, which allowed the length of the time step to increase and to obtain a smooth and clear structural response.

In the prediction, only a shrinkage parameter was set manually, and all remaining material parameters used recommended values (*fib* [36], B3 model [37]), direct experimental measurements (tensile strength and fracture energy) or previous experience (drying creep).

Fig. 1 shows the prediction in solid lines, while the experimental data are shown using points. Conclusions of the previous paper [5] were drawn based on the measurements done within the first year, indicated by a vertical green line. Consistently with the vast majority of the graphs in this paper, Fig. 1 uses a divided horizontal axis into two halves, the first logarithmic and the second linear, with a transition time of 100 days. This setup allows us to (i) clearly present the behavior soon after the onset of drying and in the first three months, and (ii) visualize the response with respect to cycles in ambient conditions whose period is constant. A single logarithmic scale was not adopted because the data would be too packed for longer durations of drying and too noisy due to cyclic conditions.

After the first year of drying (as marked by a light green vertical line in Fig. 1), the ongoing measurements of the large drying beam started to deviate from the trend given by the numerical prediction. Soon, it became clear that the earlier adopted simplification of constant ambient humidity is no longer valid. In the first few months of drying, the experimental response was governed primarily by a steep gradient in relative humidity over the cross section and the effect of fluctuations in ambient conditions was rather superficial. Yet, after approx. 6 months of drying, the concrete surface layer had equilibrated with the relative humidity of the ambient environment. As a consequence, the response became more sensitive to daily fluctuations, and the annual variations (Fig. 3) significantly impacted the global response.

After incorporating the annual cycles in relative humidity into the computational model, three major observations have been made:

Table 1
Composition of concrete used in the study.

Ingredients	Quantity [kg/m^3]
Cement CEM II/B-S 32.5R, Radotín	379
Water	185
Aggregates (fine 822, coarse 969)	1791
Superplasticizer Sika BV4	1.9

Table 2
Concrete mechanical properties at the age of 27 days.

Property	Unit	Value
Compressive strength, f_c	MPa	36.8 ± 1.4
Young's modulus, E	GPa	30.3 ± 0.3
Tensile strength, f_t	MPa	3.38 ± 0.45
Fracture energy, G_f	N/m	150 ± 21

(i) decrease in relative humidity causes drying creep but the additional creep due to humidity cycles is overestimated,
(ii) non-symmetric drying causes the evolution of deflection that cannot be captured using the Bažant-Najjar model for moisture diffusion [3],
(iii) dependence of shrinkage strain on relative humidity cannot be simplified as linear.

The objective of the present research is to investigate the overall time-dependent behavior of drying concrete specimens, accounting for the response to annual humidity cycles, and addressing the aforementioned statements. In addition, the paper also presents a methodology for efficiently combining the experimental measurements on the concrete beams, and assessing the accuracy of the measuring methods involved.

2. Material and methodology

2.1. Experimental setup

All specimens in this study were produced from a single batch of ready-mix concrete, the composition of which is detailed in Table 1. A relatively high water-to-cement ratio of $w/c = 0.49$ was chosen to ensure adequate workability without excessive admixtures and minimize autogenous shrinkage. All specimens were moist-cured for one month, followed by demolding and preparation of the final setup.

Detailed information on the composition, material properties, and details of the experimental setup is available in [5]. Table 2 lists the fundamental mechanical properties of the concrete measured at 27 days. The compressive strength and Young's modulus were determined using cylindrical specimens of size $\varnothing 150 \times 300$ mm, following EN 12390-13 [38] and EN 12390-3 [39].

Exploring the time-dependent behavior of plain concrete beams with varying sizes and sealing configurations (Fig. 2) was the central focus of the experimental program. Three identical specimens were produced for each configuration to evaluate variability, labeled A, B, and C (from front to back). Table 3 provides a summary of these configurations. All beams have a thickness of 0.1 m, and their lateral sides (front, back, left, and right, as shown in Fig. 2) were sealed with 1 layer of self-adhesive 0.030 mm thick aluminum foil, 1 layer of polypropylene tape and two more layers of aluminum foil. The sealing process took six days, after which the beams were loaded at a concrete age of $t' = 34$ days. Measurements of moisture loss on sealed cubes prove that after 5 years the sealing setup is still functional. To minimize a safety threat associated with a brittle failure of the beams, a 4 mm or 5 mm diameter (according to specimen size) threaded steel bar is embedded in the center of the cross section to minimize its restraining effect.

The loading is imposed primarily due to the self-weight of the concrete beams, except for the largest specimens designated as '200 Top', which were additionally loaded with 2×30 kg weights placed 0.6 m from the supports. The geometry and loading conditions were designed to achieve a similar magnitude of initial compressive and tensile normal stresses resulting from bending ($\sigma_x = 1.035$–1.078 MPa) and a quasi-elastic deflection ranging from 0.34 to 0.47 mm. In most cases, however, most of the deflection is attributed to the non-symmetric distribution of drying shrinkage.

The experiment is located in the large laboratory hall. As shown in Fig. 3, the ambient conditions are subject to annual but also daily

Fig. 2. Set of 7×3 beams under continuous loading, with spans ranging from 1.75 m to 3.0 m.

Table 3
Setup of the drying beams with permanent loading, rows correspond to Fig. 2.

Label	Height [mm]	Span [mm]	Length [mm]	Drying
100 Top	100	2 500	2 700	Top
100 Sealed	100	2 500	2 700	Sealed
100 Bottom	100	2 500	2 700	Bottom
100 Both	100	2 500	2 700	Top + bottom
50 Top	50	1 750	1 950	Top
200 Top	200	3 000	3 200	Top
150 Top	150	3 000	3 200	Top

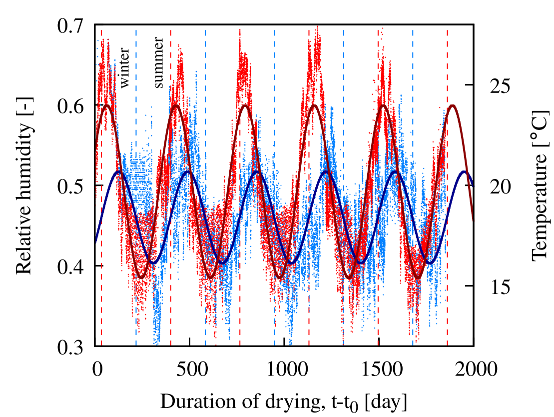

Fig. 3. Evolution of ambient relative humidity (blue, primary vertical axis) and temperature (red, secondary vertical axis) and their approximation with sine functions with a 1-year period. (For interpretation of the references to color in this figure legend, the reader is referred to the web version of this article.)

fluctuations (lower temperature dropping below 15 °C during weekends in winter and approaching 30 °C in summer). On average, the relative humidity was 46% and the temperature 19.7 °C. The least-square fit of the ambient conditions with a sine function and a period of 365 days determined the amplitude for humidity as 5.7% and for temperature 4.3 °C.

2.2. Vertical deflection of large concrete beams

Three different measuring techniques determined the evolution of the vertical displacement of the beams:

(i) Up to $t-t' = 1250$ days, five digital indicators (Mitutoyo 575-121 with a range of 25.4 mm and an accuracy of 0.02 mm) mounted on an aluminum extrusion profile [5] were used exclusively on the front specimens (A); see Fig. 4, left. The positions corresponded to the midspan of the beams at distances of 0.875 m, 1 m, 1.25 m, and 1.5 m from the left support, as well as at 1.625 m, which mirrors the sensor at 0.875 m for beams with $L = 2.5$ m. Measurements were initially taken at intervals of 1 week, later extended to 2 weeks.

(ii) Digital image correlation (DIC) provided the evolution of vertical displacement at mid- and quarterspans [40] until $t-t' = 732$ days on all specimens (A, B, C). The sampling rate was variable and decreased from 2 min to daily readings. DIC measurements were carried using an in-house PyVEx software, thoroughly described in our previous paper [40]. The software leverages a lightweight, open source approach based on the discrete Fourier transform (DFT) to efficiently evaluate displacements at discrete locations, particularly for large image sequences. Using DFT-based image registration with subpixel accuracy, PyVEx achieves faster and less user-intensive displacement measurements compared to traditional methods, focusing on specific points of interest rather than full-field analysis. Despite variable illumination conditions caused by natural lighting through the window, the correlation function normalizes pixel intensities within the region of interest, ensuring that lighting variations did not compromise the displacement measurements. However, slight fluctuations in temperature subtly affected the geometry of the objective lens, introducing unwanted scatter in the displacement data. This scatter was negligible for measurements with relatively significant vertical displacements, but adversely affected the accuracy of longitudinal measurements.

(iii) Automatic displacement sensors (MMR10-12, effective stroke 12.7 mm, total resistance 10 kΩ) were post-mounted at midspans of all beams and with a 30-min interval monitor vertical deflection of all beams (A, B, C) after $t - t' = 430$ days.

The list above indicates a large quantity of experimental data obtained at different locations, at different times, and on various specimens. It is desirable to efficiently combine the measured data to (i) assess the accuracy of the individual measuring techniques, (ii) estimate the variability in response of different loading setups and material behavior, and finally, (iii) provide a reference for the computational modeling.

The experimental methods did not allow us to measure the instantaneous deflection due to self-weight accurately. The initial offset was set to a theoretical deflection (according to beam theory) corresponding to the measured material stiffness, $E = 30.3$ GPa.

2.3. Data processing methodology

In all the investigated loading scenarios presented in Table 3, the total vertical deflection of the beam w can be, assuming linear material response over the beams' length, written as a contribution due to permanent loading w_f and shrinkage w_{sh}

$$w(x,t) = w_f(x,t) + w_{\text{sh}}(x,t) \tag{1}$$

Presumption of uniform properties over the length of the beam allows to assume constant curvature due to shrinkage κ_{sh}; therefore, the resulting deflection can be expressed in terms of the distance from the support, x, and the span L as

$$w_{\text{sh}}(x,t) = \kappa_{\text{sh}}(t)\frac{x\,(L-x)}{2} \tag{2}$$

Neglecting the contribution of 0.1 m free ends behind the supports, the deflection due to constant distributed loading with intensity f is given by

$$w_f(x,t) = J(t,t')\frac{f}{24I}\left[x^4 - 2Lx^3 + L^3x\right] \tag{3}$$

where I is the moment of inertia, and $J(t,t')$ is the total compliance function in bending (treated as uniform over the beam's length), which lumps together not only non-uniform material compliance over the cross section height (caused by dependence on humidity which is nonuniform), but also contribution due to microcracking.

Normalized plots of the two functions $w_{\text{sh}}(x)$(2) and $w_f(x)$(3) are shown in Fig. 5. The maximum difference between these two functions at the measurement locations marked by the color circles does not exceed 5%.

Except for the beams with no drying (100 Sealed) or symmetric drying (100 Both), the deflection w_{sh} becomes dominant after a certain time over the deflection due to transverse loading, w_f. Similarity of the functions w_{sh} and w_f in the region of interest and the prevailing influence of deflection due to non-symmetric shrinkage motivates us to relate the total displacement to the time-evolving average curvature $\kappa(t)$ simplified as constant over the beams' length.

$$w(x,t) \approx \kappa(t)\frac{x\,(L-x)}{2} \tag{4}$$

The validity of this approach is illustrated on beam 150 Top A whose deflections measured at five different locations (Fig. 4, left) are transformed to average curvature using (4) and shown in Fig. 4, right. The data series exhibit negligible scatter, which not only justifies the present approach and supports the accuracy of the measurements, but also proves uniform material behavior in the central region of the beam. Any suspicious deviation from the average curvature might indicate strain localization (i.e., tensile crack) and needs to be examined to prevent misinterpretation of the measured data and also to prevent possible collapse of the beam.

Data processing methodology was similar to all measuring techniques and is summarized below.

(i) At all measurement locations, the curvature is evaluated from the vertical deflection using (4).

(ii) The mean value of the curvature and its standard deviation is calculated for each specimen. To do that, the individual values of curvature from (i) are supplemented with the weights corresponding to a normalized theoretical deflection assuming constant curvature.

(iii) The values from (ii) are resampled to 100 times of interest (TOI), whose spacing forms a geometric progression starting from $\Delta t = 0.01$ day and the ratio 1.2 until $\Delta t = 30$ days which is then kept fixed.

- Digital indicators: linear interpolation is used due to the limited number of measurements.
- DIC and automatic displacement sensors: averaging over the time interval is employed to eliminate the noise.

(iv) For every set of beams with the same geometry and sealing configuration, the mean value of the curvature and its standard deviation is calculated using the TOI data from (iii).

- DIC: to reflect the variations of the individual beams, weights calculated from their standard deviations are used.

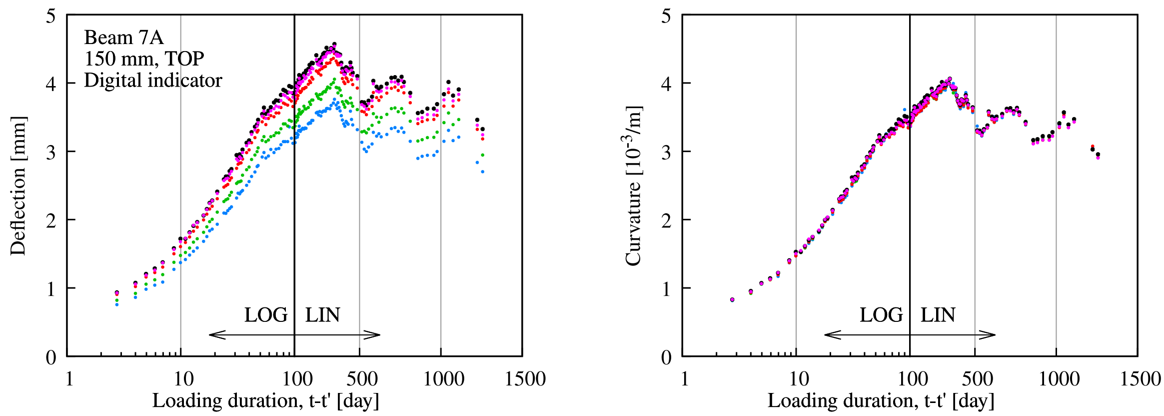

Fig. 4. Measurement of vertical deflection on beam 150 Top (A) with a set of five digital indicators (left) and the corresponding average curvature (right).

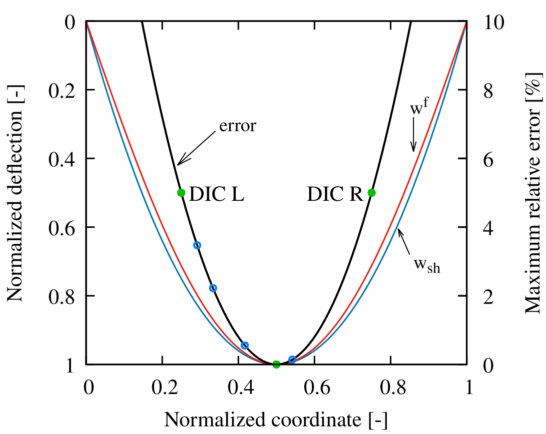

Fig. 5. Normalized deflection due to non-symmetric shrinkage w_{sh}(2) and due to constant distributed loading w_f(3). Circular marks correspond to the positions of the measurements on the beam with $L = 3$ m. In the region of interest, the maximum error (dashed line) does not exceed 5%.

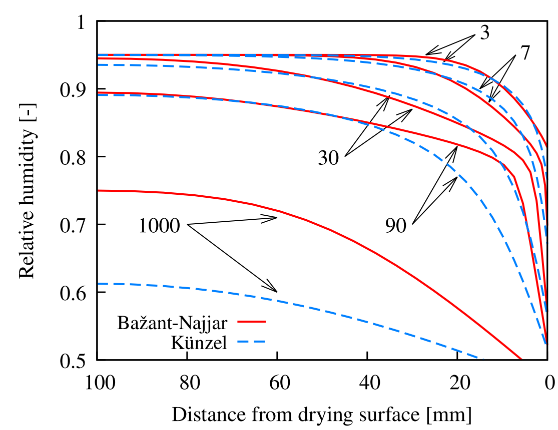

Fig. 6. Comparison of moisture profiles at indicated durations of drying (in days) according to the model by Bažant and Najjar (solid red lines) and by Künzel (blue dashed lines).

The mean values in the resulting data set characterize the general behavior of the beams, the standard deviation helps to assess the accuracy of different measurement techniques and to evaluate the influence of material variability on the measured response.

2.4. Material models and modeling

The evolution of annual humidity cycles is approximated by a sine function as shown in Fig. 3 in the solid blue line and specified in Table 4. More detailed variations in humidity and incorporation of the heat transport problem would have resulted not only in strict requirements on the maximum time step length to provide numerical stability, but would also have incorporated more expressions and material parameters establishing cross-coupling between heat and moisture problems.

The temperature is prescribed explicitly and uniformly throughout the domain using a sine function shown in Fig. 3 in solid red line and specified in Table 4. This measure is implemented primarily to ensure numerical stability even with longer time steps and is justified by much higher thermal conductivity compared to moisture permeability. This approach allows us to reflect different drying rates during summer and winter periods. The experimental data presented in this paper are temperature compensated, and so thermal dilation is not modeled.

All coupled finite element simulations were conducted using a staggered approach, where the humidity transport analysis was performed before the mechanical analysis (one-way coupling only). These simulations used the open source finite element solver OOFEM [30,31].

The nonmonotonous and highly nonlinear derivative of the diffusivity function proposed in the model by Bažant and Najjar [3] caused a structural response that had, even under constant ambient conditions, two maxima [5] (solid lines in Fig. 1) which are not observed in experiments. For this reason, a different and more general approach proposed by Künzel [4] is adopted instead. Fig. 6 presents an example in which the distributions of relative humidity for several durations of drying (indicated by arrows and a label in days) and computed with the models by Bažant and Najjar, and Künzel. In this figure, the left and right edges correspond to the sealed and exposed surfaces, respectively, in a 100 mm thick specimen. Strong differences arise approximately after the first 7 days of drying, when the moisture profiles according to Bažant and Najjar tend to become highly nonlinear due to the strong jump in moisture diffusivity around the relative humidity in pores $h \approx h_c = 0.8$ (diffusivity below this threshold is 20× smaller than above this limit). This threshold value of relative humidity consequently divides the profile into two parts: an extremely steep part close to the drying surface and a flat and slowly decreasing plateau in the remaining part of the cross section. Although the outer part close to the surface is drying only very slowly between 30 and 90 days, the relative humidity of pores in the central part drops significantly, which is associated with a local minimum of the deflection in Fig. 1. Once the relative humidity h drops slightly below the threshold value of h_c, the moisture diffusivity becomes almost constant, and so the solution becomes almost linear again.

Table 4
Material parameters and evolution of ambient conditions for the transport subproblem.

	Parameter	Unit	Value
Moisture transport (Künzel)	A	kg m^{-2} day$^{-0.5}$	0.6
	w_f	kg m^{-3}	110
	q	–	4
	μ	–	100
Sorption isotherm (van Genuchten)	b	–	6.126
	m	–	0.331
Boundary condition	f	kg m^{-2} day^{-1}	0.2
	$h_{\mathrm{env}} = 0.46 + 0.057\sin(2\pi(t-34.8)/365)$		
	$T_{\mathrm{env}} = 292.8 + 4.3\sin(2\pi(t+28.0)/365)$ K		

The model by Künzel was developed and validated for transport tasks similar to the current experiment and its formulation is summarized below. With the assumption of constant temperature and zero moisture sink, justified by a high water-to-cement ratio $w/c = 0.49$, the moisture balance equation reads

$$\frac{\mathrm{d}w}{\mathrm{d}h} \cdot \frac{\mathrm{d}h}{\mathrm{d}t} = \nabla \cdot \left[\left(k_\eta(T) D_w \frac{\mathrm{d}w}{\mathrm{d}h} + \delta_p(T) p_{sat} \right) \nabla h \right] \tag{5}$$

where w [kg m^{-3}] is the moisture content, h [–] is the relative humidity in pores, $k_\eta(T)$ is a relative temperature-dependent coefficient, D_w [m^{2}day^{-1}] is the capillary transport coefficient, δ [kg m^{-1} day^{-1} Pa^{-1}] is the water vapor diffusion coefficient of the building material, p_{sat} [Pa] is the saturation vapor pressure, and $\nabla\cdot$ and ∇ are the divergence and gradient operators, respectively.

At higher values of relative humidity, capillary transport is dominant, and the expression for the transport coefficient reads

$$D_w = 3.8 \left(\frac{A}{w_f} \right)^2 10^{q\left(\frac{w}{w_f}-1\right)} \tag{6}$$

where A [kg m^{-2} day$^{-0.5}$] is the water absorption coefficient, q is a parameter defining nonlinearity of the exponential function, and w_f [kg m^{-3}] is the moisture content at free saturation. The temperature dependence of the capillary coefficient is established via a multiplicative dimensionless term

$$k_\eta = \left(\frac{64}{T-229} \right)^{-1.532} \tag{7}$$

where T is the temperature in Kelvin.

The water vapor permeability of the building material becomes dominant over capillary transport at lower levels of relative humidity and is defined as

$$\delta_p = \frac{2 \cdot 86400 \cdot T^{0.81}}{101325 \cdot \mu} \times 10^{-7} \tag{8}$$

where μ [–] is the water vapor diffusion resistance.

The water vapor saturation pressure in (5) is approximated as

$$p_{sat}(T) = 611 \exp\left(\frac{17.08(T-273.15)}{T-39.} \right) \tag{9}$$

The sorption isotherm is idealized as non-aging and temperature-independent. A flexible expression proposed by van Genuchten [41]

$$w(h) = w_f \left[1 + (-b \ln h)^{\frac{1}{1-m}} \right]^{-m} \tag{10}$$

is used to relate the moisture content w with the relative humidity h using two dimensionless fitting parameters m and b and the saturation moisture content w_f, estimated from the moisture balance of the concrete cylinders in the initial state and in equilibrium with ambient conditions. The least squares fit of the experimental data in Fig. 7 determined $b = 6.126$ and $m = 0.331$. The initial value of relative humidity of pores was assumed to be 95%. A mixed boundary condition for the flux J [kg m^{-2} day^{-1}]

$$J = f(h_{\mathrm{env}} - h) \tag{11}$$

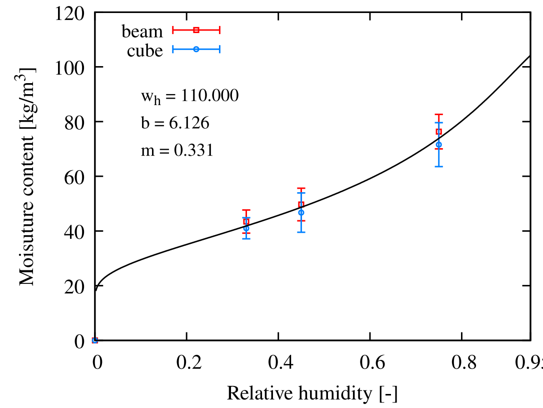

Fig. 7. Fit of Experimental data with van Genuchten expression for sorption isotherm.

was assigned to the exposed surfaces where h_{env} is the ambient relative humidity and f is the surface factor [kg m^{-2} day^{-1}].

As in the previous blind prediction study [5], the time-dependent behavior of concrete in structural analysis is based on the modified Microprestress-Solidification theory. A comparison between the numerical results and the experimental data presented in Section 3 indicates that certain modifications related to shrinkage and drying creep under cyclic humidity conditions are necessary.

The model integrates a linear viscoelastic aging material described by the MPS theory [42], which has been modified to capture the size effect on drying creep accurately [32,33], along with a softening smeared cracking model in tension. Tensile softening begins when the maximum principal stress reaches the tensile strength; subsequently, the orientation of the crack plane remains fixed [34]. Regularization is performed using the crack band approach [35].

The viscoelastic and cracking models are connected in series, ensuring that the total deformation is the sum of both contributions while the stresses remain equal. The model is formulated incrementally, with the new stress vector at time step $i+1$ computed from the previous equilibrated stress vector σ_i and the product of the viscoelastic stiffness matrix $\bar{\mathbf{D}}_{ve}$ and the increment of the stress-related strain vector $\Delta\varepsilon_\sigma$:

$$\sigma_{i+1} = \sigma_i + \bar{\mathbf{D}}_{ve}\Delta\varepsilon_\sigma = \sigma_i + \bar{\mathbf{D}}_{ve}\left(\Delta\varepsilon_{tot} - \Delta\varepsilon'' - \Delta\varepsilon_{\mathrm{sh}} - \Delta\varepsilon_T - \Delta\varepsilon_{cr}\right) \tag{12}$$

In this equation, $\Delta\varepsilon_{tot}$ is the total strain increment, $\Delta\varepsilon''$ represents the creep strain increment, $\Delta\varepsilon_{\mathrm{sh}}$ is the shrinkage strain increment, $\Delta\varepsilon_T$ is the thermal dilation increment, and $\Delta\varepsilon_{cr}$ is the cracking strain increment.

Under hygrally sealed conditions and constant room temperature, the model simplifies to the basic creep compliance function of the B3 model [37], which is fully described by only four parameters, q_1 to q_4. Their values, summarized in Table 5, were estimated based on the concrete composition (including total cement content and slag) and the compressive strength at 1 month.

Drying in concrete leads to both stress-dependent and stress-independent deformations. According to the MPS theory, the evolution of additional compliance due to drying is characterized by an irreversible strain captured by an aging dashpot whose viscosity η_f depends on an internal humidity- and a temperature-dependent quantity called microprestress. Changes in relative humidity and temperature, whether increasing or decreasing, generate microprestress, which gradually relaxes under constant conditions. In [43] it was shown that microprestress and a redundant material parameter can be eliminated from the formulation and replaced with viscosity. To correct the size effect on drying creep in the original MPS model, setting the exponent p in the governing equation for microprestress to $p = \infty$ is effective [32,33]. Under constant temperature, the governing equation for the viscosity η_f becomes

$$\dot{\eta}_f + k_3 \left| \frac{\dot{h}}{h} \right| \eta_f^{\tilde{p}} = \frac{\psi_S}{q_4} \tag{13}$$

Table 5
Material parameters for the structural sub-problem.

	Parameter	Unit	Value
	ρ	kN m^{-3}	23
Solidification theory	q_1	MPa^{-1}	20.91×10^{-6}
	q_2	MPa^{-1}	140.8×10^{-6}
	q_3	MPa^{-1}	2.32×10^{-6}
	q_4	MPa^{-1}	6.85×10^{-6}
Microprestress: equivalent times	α_E	–	10.
	α_R	–	0.1
	α_S	–	0.1
Microprestress: drying creep	$\tilde{p}$	–	1.
	k_3	–	15.
	$k_{h,c}$	–	0.3
Microprestress: drying shrinkage	k_{sh}	–	2×10^{-3}
	r_{sh}	–	0.5
	h_{sh}	–	0.8
Tensile cracking	f_t	MPa	3.4
	G_f	N/m	150.

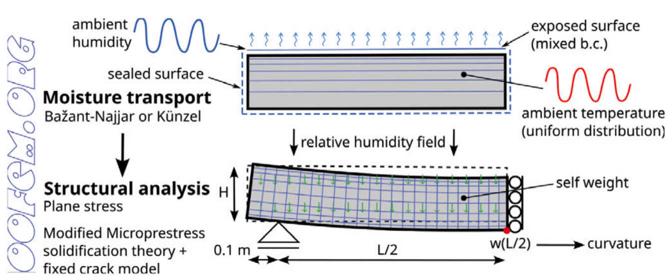

Fig. 8. Schematic representation of the modeling workflow and FE models for concrete beam '100 Top'.

where $\tilde{p} = p/(p-1) = 1$, and k_3 is a dimensionless parameter. In the prediction based on the one-year data [5], k_3 was set to 30.

The viscoelastic behavior under variable humidity also depends on three parameters α_E, α_R, and α_S, which determine the evolution of transformed times based on the history of relative humidity at each material point. These parameters were assigned their default values (Table 5).

According to the MPS model, the rate of drying shrinkage is directly related to the rate of change of relative humidity by

$$\dot{\varepsilon}_{sh} = k_{sh}\dot{h} \tag{14}$$

where k_{sh} is the shrinkage parameter. Autogenous shrinkage, which results in uniform shrinkage without causing deflection, was not considered here.

The smeared cracking extension was calibrated by fitting the experimental results of conventional bending tests with and without notch, the parameters of the softening law were identified as $f_t = 3.4$ MPa and $G_f = 140$ N/m [5].

The computational models corresponded to the symmetric half of the beams with homogeneous material properties, as schematically shown in Fig. 8. In the transport problem, due to the 1-D nature of the problem, the mesh was composed only of 20 quadrilateral elements with linear approximation of relative humidity and with increasing size from the drying surface. The structural sub-problem used a structured mesh consisting of quadrilaterals with a linear displacement approximation. In the axial direction of the beam, the element size was uniform, 10 mm. In contrast, in the transverse direction, the mesh was refined toward the surfaces, and 14–16 elements were used per height (according to the geometry).

3. Results and discussion

3.1. Accuracy of the measuring techniques

All three experimental methods used for measuring vertical deflection of the beams have demonstrated good performance. Here, the quantity used to characterize the accuracy of the measurement is taken as the deviation from the average curvature. Therefore, only the methods that use more than one measurement location can indicate the development of measuring accuracy or its consistency over time; in the present case it is the set of five digital indicators and DIC with three measurement locations.

Fig. 9 shows this trend for the front specimens ('A'). Note that the measuring locations of the two methods did not coincide. The standard deviation of the curvature when measured with a set of five digital indicators is very satisfactory except for the shortest specimens, but this is primarily due to unfavorable measuring locations whose distance from the left support was kept fixed and thus identical for all specimens.

Initially, the error evaluated with DIC was very similar for all specimens. However, after approximately 3 months, the error started to increase rapidly, which was caused by a combination of more factors: out-of-focus scene caused by temperature,[1] poor lighting conditions, and unintentional manipulation with the DIC markers.

Readings done with automatic displacement sensors offer accuracy superior to DIC and digital indicators. The readings are very consistent among identical specimens and even enable one to register response to daily fluctuations in ambient humidity. The only drawback is the high number of sensors needed to equip each beam should these measurements detect localized concrete cracking, which is only possible if the deflection is measured at multiple locations.

Based on these observations, the best approach to instrument such experiment in terms of both cost-efficiency and accuracy seems to be the combination of two methods, namely DIC (inexpensive, measurement at different locations to detect suspicious behavior such as localized cracking) and three automatic displacement sensors (two for axial shortening, one for vertical midspan deflection). Provided the ambient conditions are stable and the DIC plates are solid, the DIC accuracy is likely to remain good throughout the experiment.

3.2. Behavior of the concrete beams

The processed experimental data of the concrete beams resampled to 100 times of interest are shown in Fig. 10 for h = 100 mm and different sealing configurations and in Fig. 11 for different heights h and drying from the top surface. Different colors in the plots are used to distinguish the response of the geometrically identical specimens A, B, and C (front, middle, and back). Circular red markers correspond to measurements using digital indicators in series A (front specimens), solid lines with shades show the mean and standard deviation of the individual samples measured by DIC (up to $t - t' = 732$ days), and dashed lines mark automatic measurements with displacement sensors at the mid-span (from $t - t' = 430$ days onward).

The reference sealed beams labeled '100 Sealed' loaded in bending exhibit a slightly faster initial creep rate than the prismatic columns loaded in axial compression, which was in agreement with the blind prediction of the B3 model. The excessive compliance can be attributed to microcracking as demonstrated later in Fig. 18. After approximately 1 year, the creep rate (and also 'autogenous' shrinkage of the companion specimen) increased—probably due to moisture leakage where the strain gauges are attached. Therefore, this increase was not observed in the beam specimens and is not considered.

The maximum curvature measured is inversely proportional to the size of the specimen and its main source is nonsymmetric drying shrinkage. Initially, the behavior is driven by a steep gradient of the

[1] Influence of temperature on DIC measurements has completely eliminated the possibility of evaluating axial shortening of the beams.

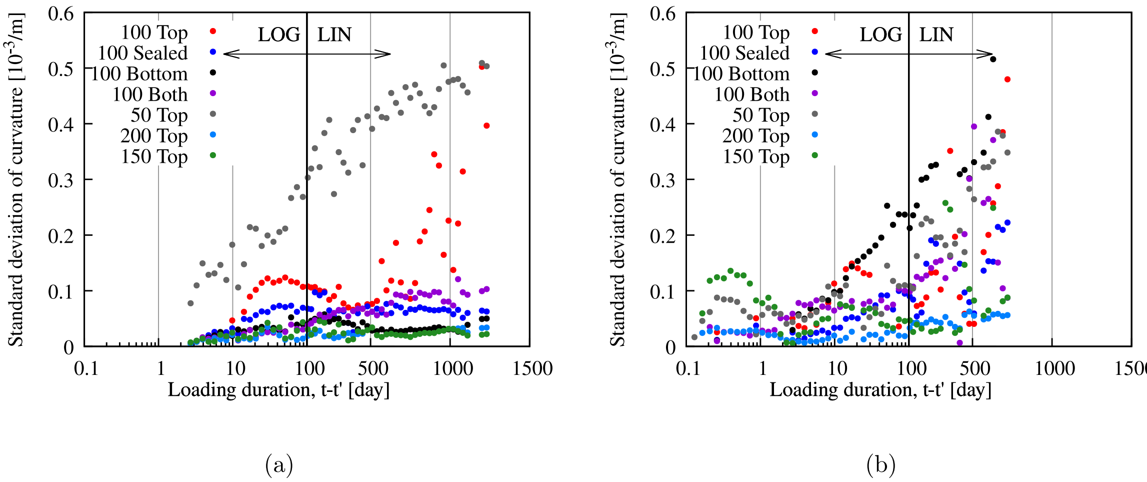

Fig. 9. The standard deviation of curvature evaluated from vertical deflections of 'A' specimens measured at different locations with a set of five digital indicators (a) and DIC (b).

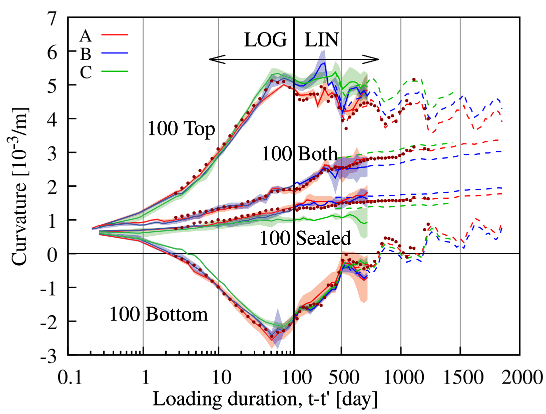

Fig. 10. Evolution of curvature of beams with a height of 100 mm and **different sealing configurations**. Colors distinguish individual specimens (A, B, C). Points = digital indicators (series A only), solid lines with shades = mean and standard deviation with DIC, dashed lines = displacement sensors. (For interpretation of the references to color in this figure legend, the reader is referred to the web version of this article.)

moisture profile, which develops over the depth of the beam and is approximately terminated by reaching the maximum value. This transition time is size-dependent. Afterward, the response starts to be sensitive to variations in ambient conditions. Naturally, this sensitivity decreases with specimen size.

Fig. 11 shows that the experimental scatter is strongly size-dependent. The responses of the individual specimens from the series '150 Top' and '200 Top' are almost identical throughout the course of the experiment. Differences in the behavior of smaller specimens arise already after approx. 1 week ('50 Top') and approx. 1 month ('100 Top') when the deflection is close to its maximum. Afterward, the trend remains consistent but is offset by a constant. This variability can probably be attributed to only several millimeters thin layer of concrete surface exposed to drying, whose heterogeneity and different fractions of mortar and aggregates give rise to different overall shrinkage. The microcracking that develops is almost uniform in length. This is justified by a small variation from the average curvature, which would not have been the case if the damage were localized.

Even in the case of 100 mm deep beams exposed to drying from the bottom surface ('100 Bottom'), the variation of the curvature is very small and the trend is even more consistent compared to their counterparts drying from the top surface ('100 Top'), see Fig. 10. The combination of loading due to self-weight and drying, which is in these two cases opposite, causes only minor differences in the integrity of the surface layer because the maximum curvature occurring approximately at $t - t' = 2$ months is symmetric with respect to the response of the sealed specimens. In addition, the effect of annual variations in ambient conditions leads to comparable responses.

In the case of symmetric drying ('100 Both'), which leads to the highest internal restraint to drying shrinkage, the compliance rate is higher than in the case of sealed concrete ('100 Sealed'). This difference comes from two sources: microcracking (mainly up to 10 days), which is followed by drying creep once the drying front penetrates deeper into the concrete. Interestingly, the creep rate of the almost dry concrete is higher than the basic creep, which is the opposite of the other observations [44–46], but this can be attributed to different degrees of hydration (solidified volume) in the two cases and to the reduced bending stiffness of the drying specimen caused by restrained microcracking.

The resulting data set of the large beams is shown in Fig. 12. This figure combines DIC measurements (solid lines with shades) and automatic measurements at the midspan (dashed lines with shades). Shaded areas denote the standard deviation, which was in the case of DIC computed using not only data from 3 geometrically identical specimens but also by considering variations of the individual specimens. In the case of the automatic mid-span measurements, the standard deviation almost does not evolve as the vertical offset of the data series is practically constant after 1 year of drying.

In addition to the data presented on concrete beams, the sequential improvement and validation of the material model used data from complementary experiments whose description is presented in the preceding publication [5].

- The total shrinkage (Fig. 14) was measured on prisms $100 \times 100 \times 300$ mm with two lateral sides exposed to drying. Deformation that had occurred before the age of 28 days when drying began was not recorded.
- The axial and bending compliance was obtained from an eccentric creep test (Fig. 15), which used geometrically identical prisms loaded by a 50 kN force with 16 mm eccentricity to produce 10 MPa and 0 MPa compression at the drying surfaces.
- Moisture loss measurements (Fig. 21) used cylinders with sealed circumference and heights ranging from 25 mm to 200 mm. The two smallest heights were not considered due to significant material inhomogeneity and carbonation shrinkage, which manifested after the first year of drying.

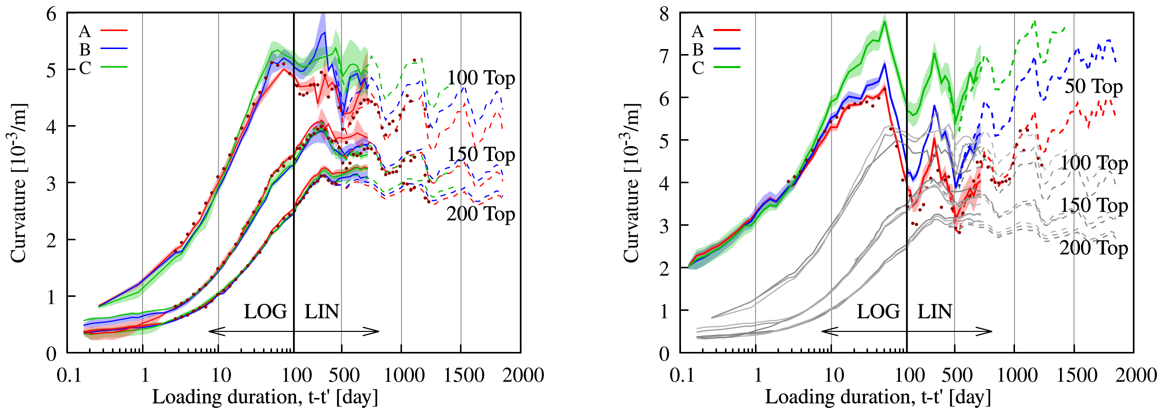

Fig. 11. Evolution of curvature of beams with **different heights and drying from the top surface**. Colors distinguish individual specimens (A, B, C). Points = digital indicators (series A only), solid lines with shades = mean and standard deviation with DIC (until $t - t' = 732$ days), dashed lines = displacement sensors (from $t - t' = 430$ days onwards). (For interpretation of the references to color in this figure legend, the reader is referred to the web version of this article.)

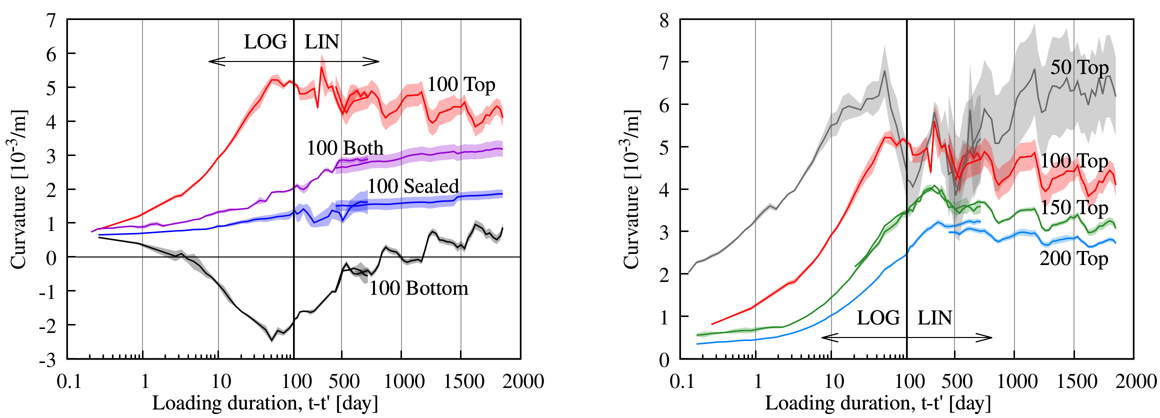

Fig. 12. Final experimental data set: evolution of curvature and its standard deviation (shades) for specimens with different sealing configurations (left) and different heights and drying from the top surface.

3.3. MPS improvement

When modeling the behavior of concrete beams exposed to nonsymmetric drying, the Bažant-Najjar model for moisture diffusion leads to the evolution of transverse deflection, which contradicts experimental observations as shown in Fig. 1. Suppose that the Künzel model is used instead, and the MPS model for the structural sub-problem is preserved. In that case, the model's response significantly improves and the second maximum, which exceeds the magnitude of the first one, vanishes.

Despite this partial success, the results indicate that both the sensitivity to shrinkage established based on 1-year data by the parameter k_{sh}(14) and the drying creep, and its rate under ambient humidity cycles, are overestimated. The response of the model is shown in dotted lines labeled '(A) prediction' in Figs. 13–15 which show the evolution of curvature, total shrinkage and compliance under eccentric loading, respectively. In these figures, annual cycles of ambient conditions are considered in the FE analysis. To emphasize the subsequent model calibration, capital letters A, B, C are used to label the numerical model results.

Although creep and shrinkage occur simultaneously, their interaction in the present experiments is rather limited, which allows us to calibrate these phenomena subsequently; drying shrinkage is analyzed first.

A simple reduction of the shrinkage parameter k_{sh} used in the blind prediction to 60% would have satisfied the value of the ultimate shrinkage, whose mean value stabilizes around approx. 600 $\mu\varepsilon$ instead of 1000 $\mu\varepsilon$ (Fig. 14) but would have caused an excessive delay in its development. Instead, inspired by the results of the mesoscale simulations and experimental evidence [6,47–49], the dependence of the nonlinear dependence between the shrinkage strain and the relative humidity of pores is established. This nonlinearity arises jointly from the nonlinear dependence of the drying shrinkage of cement paste under uniform drying conditions [8,50–53] and the concrete mesostructure which produces a non-uniform stress distribution and causes creep and microracking [54–56]. In order not to introduce an excessive number of parameters, a shrinkage reduction factor $r_{sh} = 0.5$ is introduced that becomes activated once the relative humidity of pores drops below its threshold value $h_{sh} = 0.8$ which is consistent with the findings in [6].

$$\dot{\varepsilon}_{sh} = \begin{cases} k_{sh}\dot{h} & \text{if } h \geq h_{sh} \\ k_{sh} r_{sh} \dot{h} & \text{otherwise} \end{cases} \tag{15}$$

In Figs. 13 and 14, the results obtained with the nonlinear dependence of shrinkage on relative humidity are labeled '(B) k_{sh}(h)' and shown in thin dashed lines. With this improvement, the ultimate shrinkage and the effect of annual humidity cycles on shrinkage are captured realistically—both in the case of axial shrinkage under symmetric drying conditions (Fig. 14) and curvature of nonsymmetrically drying beam (red color in Fig. 13). It needs to be emphasized that the temperature effect on relative humidity of pores during the ambient cycles was not considered. Introduction of the shrinkage reduction factor has no visible effect on the curvature of symmetrically drying beam and on the creep response of prism subject to eccentric compression, which implies that with the present modeling approach, the damage of the surface layer is not too sensitive on the exact shape of the drying shrinkage profile.

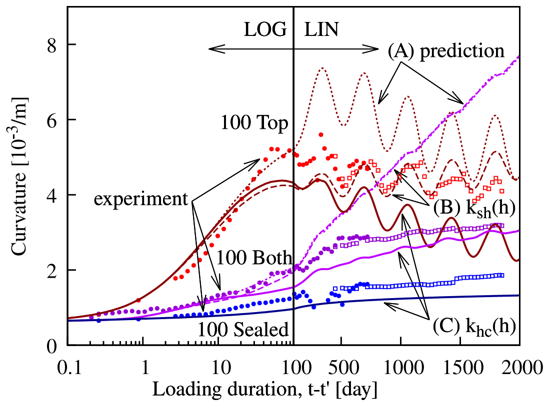

Fig. 13. Comparison of the measured average curvature of beams '100 Top', '100 Both', and '100 Sealed' (circles) with the results of FEM simulations using different approaches. A (dotted lines): Eq. (13), B (dashed lines): nonlinear shrinkage dependence (15), and C (solid lines): nonlinear shrinkage (15) and treatment creep under humidity cycles (16). (For interpretation of the references to color in this figure legend, the reader is referred to the web version of this article.)

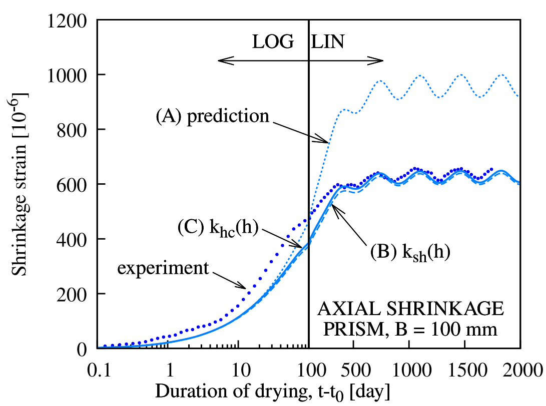

Fig. 14. The evolution of total axial shrinkage was determined from the experiment (circle marks) and using different modeling approaches (lines).

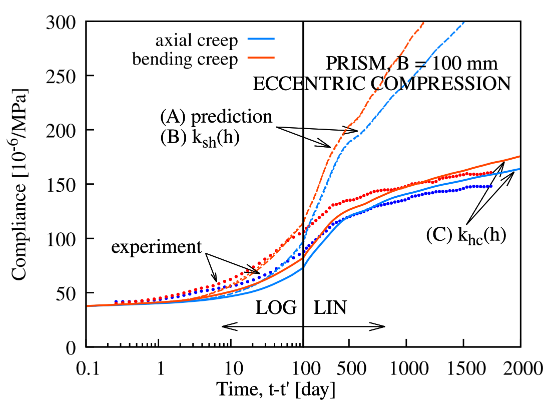

Fig. 15. Measured total axial and total bending creep of a drying prism subjected to eccentric compression (circles) and the response of different modeling approaches (lines).

After calibrating the response to drying shrinkage, drying creep is examined next. Fig. 14, which shows the axial shrinkage of a prism with notional size 100 mm, allows one to identify the instant when monotonous drying is replaced by wetting, which is manifested by a decrease in shrinkage strain and a slight swelling caused by an increase in ambient relative humidity that occurs almost exactly after 1 year of drying. In the eccentric compression creep experiment (Fig. 15), which uses the specimen with the same notional size, the transition period of 1 year suggests that the drying creep rate is overestimated under both monotonous and cyclic drying. Calibrating the drying creep under sustained drying conditions is straightforward because it is primarily controlled by the parameter k_3 set to 30 in the initial prediction. To match correct compliance after 1 year, this parameter is reduced to $k_3 = 15$.

The original formulation of the MPS model overpredicts creep rate not only in the case of variable ambient humidity, but also under periodic heating and cooling cycles. To match the experimental data of Fahmi [45], the generation of microprestress had to be reduced in subsequent thermal cycles to approximately 6% of its initial value [43]. To adapt this approach to humidity cycles, Eq. (13) is rewritten as

$$\dot{\eta_f} + k_3 k_h \left|\frac{\dot{h}}{h}\right| \eta^{\tilde{p}} = \frac{\psi_S}{q_4} \tag{16}$$

where k_h is a newly introduced history-dependent factor that becomes activated whenever the humidity becomes greater or equal to the lowest previously attained value in a given location, which can be formulated as

$$k_h = \begin{cases} 1.0 & \text{if } h = h_{\min} \text{ and } \dot{h} < 0 \\ k_{h,c} & \text{otherwise} \end{cases} \tag{17}$$

$$h_{\min}(t) = \min_{t' \le t} h(t') \tag{18}$$

Under monotonous drying, the previous equation for the flow-term viscosity (13) is restored. In the case of eccentric compression, the experimental data are captured (solid lines labeled '(C) $k_{h,c}(h)$' in Fig. 15) if (under humidity cycles) the generation of microprestress is reduced to 30% which corresponds to $k_{h,c} = 0.3$. The axial shrinkage strain is almost unaffected by this modification, Fig. 14.

In the case of the drying beams in Fig. 13, the suggested damping of the drying creep leads to satisfactory results that are marked by thick solid lines. The behavior of the beams subjected to symmetric drying (100 Both) can be divided into several stages. Until $t - t' = 10$ days, the behavior is captured correctly by the model, and the deflection increases faster than for the sealed specimen, which is due to the high internal restraint to drying shrinkage, which causes cracking in the surface layer and thereby increases compliance. Next, until $t - t' \approx 60$ days, the creep rate is underestimated by the model, and this difference is very similar to that of the sealed beam. Note that in the model, creep in tension and compression are considered equal [1,57–61]. Since the compression creep is captured correctly by the model, the source of this additional deflection can be associated with delayed cracking at the bottom fibers, where the maximum tensile stress due to bending is approximately 1 MPa. Until $t - t' \approx 1$ year, the exposed surface undergoes monotonous drying, which leads to drying creep, in this interval the creep rate matches. From 1 year onward, the surface layer undergoes humidity cycles, the creep rate damped using parameter $k_{h,c}$ is close to the experimental data. The response of the non-symmetrically drying beam '100 Top' also improves. The offset from the experimental data remains almost constant from $t - t' = 60$ days.

The response of all beams computed with the final set of parameters listed in Tables 4 and 5 and suggested improvements that introduce nonlinearity in drying shrinkage and mitigate excessive drying creep in humidity cycles is presented in Fig. 16. Considering the sequential nature of the calibration of the structural sub-problem, the agreement with the experimental data can be considered satisfactory. Optimum calibration using surrogate models based on computationally efficient low-fidelity models is currently in progress.

The most obvious shortcoming of the model is the insufficient deflection of the beams drying from the top surface, which reaches only 80% of the experimental value in all cases examined. This difference emerges shortly before reaching the maximum value, after which it is almost constant. This suggests that this difference is associated with irrecoverable deformation, i.e., creep and/or microcracking, and would

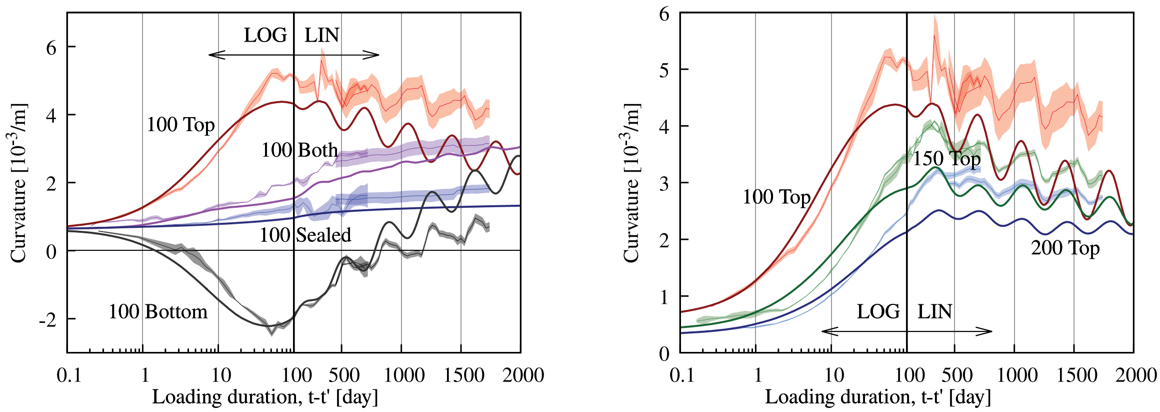

Fig. 16. The evolution of the average curvature of the beams with different sealing configurations and heights obtained with the improved model. (For interpretation of the references to color in this figure legend, the reader is referred to the web version of this article.)

explain underestimated deflection in the case of symmetric drying '100 Both' and sealed specimen '100 Sealed'.

The cycles in curvature shown in Fig. 16 caused by the annual cycles of ambient relative humidity are visually almost perfectly synchronized and are slightly lagging behind the prescribed humidity; for the present model calibration, this delay is 24 days for the specimen '100 Top' and 40.5 days for '200 Top'.

The importance of considering drying creep and tensile cracking in the material model is shown in Figs. 17 and 18, respectively. Solid color lines correspond to the reference calibrated model shown in Fig. 16 while the green dashed lines correspond to the response of a model in which drying creep or tensile cracking are not considered.

Without drying creep (Fig. 17), the most significant difference compared to the reference model is in the case of symmetric drying. Initially, the behavior is very similar, steep humidity profile together with high internal restraint caused by the cross section cause microcracking at the bottom fibers and subsequently lead to an increase in compliance. However, after approx. 2 months of drying, the humidity in the center of the cross section decreases, the cracks close, resulting in a restoration of stiffness that is after 1 year very close to that of the sealed beam and far from experimental evidence. Without considering drying creep, only the creep rate of the beams with one-sided specimens decreases.

When tensile cracking is not considered in the constitutive model (Fig. 18), the response of the beams with one-sided drying remains practically unchanged because the tensile stresses produced by the non-symmetric distribution of the shrinkage eigenstrain can be relieved by their deflection. In contrast, symmetric drying leads to a significant build-up of tension. If tensile cracking is not considered, the deflection remains identical to that of the sealed specimen for the first 10 days of drying, after which the deflection grows once drying creep becomes significant. Interestingly, the final compliance and its rate are very similar because the surface cracks eventually close.

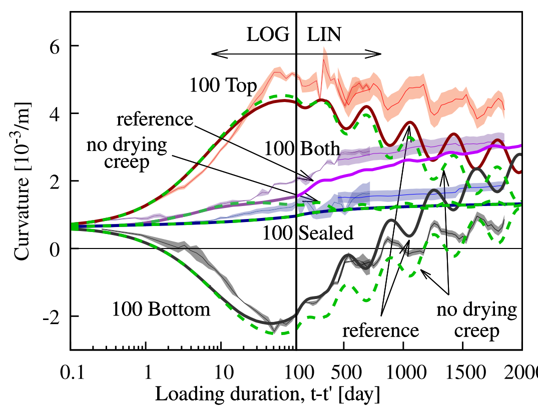

Fig. 17. Curvature of 100 mm deep beams with different sealing configurations with (solid color lines) and without (dashed green lines) considering **drying creep** in the constitutive model. (For interpretation of the references to color in this figure legend, the reader is referred to the web version of this article.)

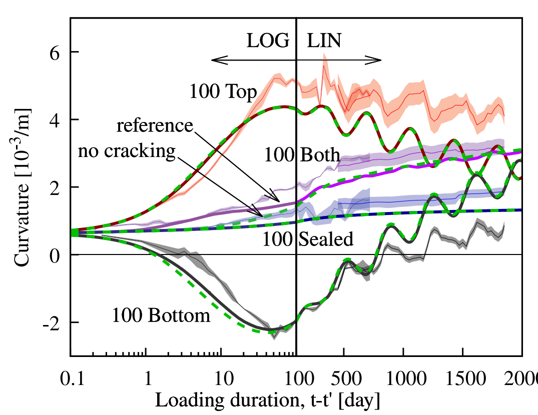

Fig. 18. The curvature of 100 mm deep beams with different sealing configurations with (solid color lines) and without (dashed green lines) considering **tensile cracking** in the constitutive model. (For interpretation of the references to color in this figure legend, the reader is referred to the web version of this article.)

3.3.1. *Effect of ambient boundary conditions*

For computational reasons and to capture the main feature of the experimental data, the results of all simulations presented used a simplified history of ambient conditions; the measured evolution of ambient relative humidity was fitted with a sine function, which was subsequently assigned as a boundary condition in the transport problem. From an engineering point of view, this simplification can be considered acceptable because the response of the model was in good agreement with the experimental observations.

Imagine a scenario if the time-stepping is refined, allowing us to prescribe the ambient conditions more accurately. Fig. 19 compares the sine fit of ambient humidity ('reference') with its 1-day, 1-week, and 1-month averages. Naturally, the finer the averaging period, the sharper the fluctuations; however, the depth they penetrate rapidly decreases with their frequency [1] and, in the present case, affects only a thin concrete cover. Therefore, their effect on the creep response in bending is much more apparent than in axial compression.

As shown in Fig. 20, the beam with its bottom surface exposed to drying exhibits very little sensitivity to the nature of the ambient conditions prescribed. This is because the exposed surface cracks, which

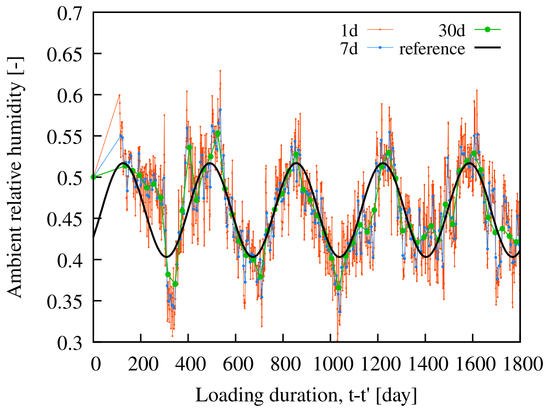

Fig. 19. Comparison of different ambient relative humidity functions used as boundary condition in moisture transport sub-problem. Smooth fit of the measured data with a sine function ('reference') is compared to 1-day, 1-week and 1-month averages marked with different colors. (For interpretation of the references to color in this figure legend, the reader is referred to the web version of this article.)

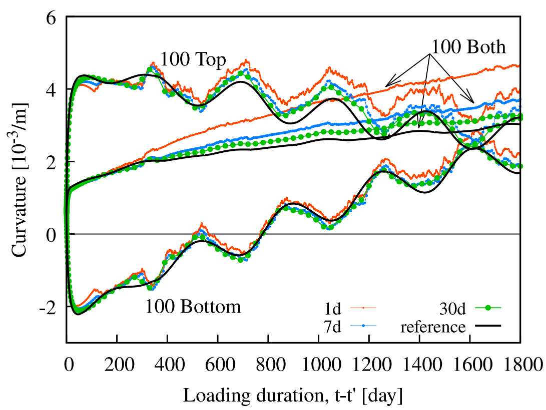

Fig. 20. Computed response of beams with 100 mm height and 2.5 m span and different sealing configurations subject to different histories of ambient relative humidity from Fig. 19, shown by different colors. (For interpretation of the references to color in this figure legend, the reader is referred to the web version of this article.)

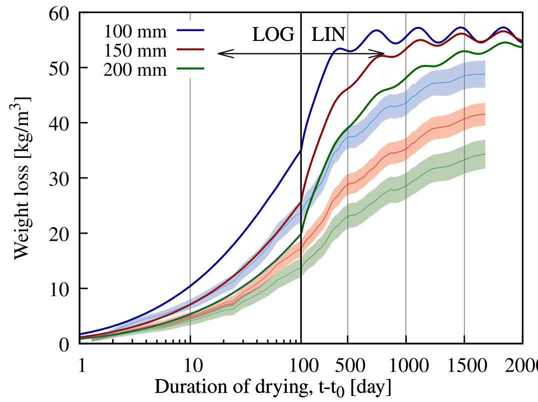

Fig. 21. Measured (lines with shades denoting ± standard deviation) and computed (smooth lines) moisture loss of concrete cylinders with different heights.

leads to stress redistribution. Oscillations in relative humidity in this (cracked) layer have very little impact on overall behavior. On the other hand, a significant increase in compliance rate can be observed after 1 and 2 years in the case of the specimen '100 Both' and '100 Top', respectively. These observations suggest that the proposed approach is not sufficiently general to be compatible with an arbitrary sampling history of ambient conditions. Therefore, it is recommended that the history of ambient conditions be first processed with a smoothing procedure.

3.4. Open questions

Although the calibrated and improved model exhibited good agreement with the data from traditional creep and shrinkage experiments as well as with the data measured on beams of different sizes and with different sealing configurations, there is one specific aspect which deserves further attention.

Similarly to blind prediction [5] that used the Bažant-Najjar model for moisture transport, there is a significant mismatch between the evolution of moisture loss and shrinkage. To match the correct development of shrinkage — both axial shrinkage in the prism and shrinkage-induced curvature in the beams — the corresponding evolution of moisture loss in cylinders with sealed circumferences and different heights is significantly faster than in the experiment, as shown in Fig. 21. This deficiency can be partially explained by a delayed hydration of the slag, which is not considered in the present model.

As the first approximation, the linear dependence of shrinkage strain on moisture loss is often assumed [1,3]. In reality, this relationship is more complex [51,62] as demonstrated, e.g., by and extensive studies of Aguilar [63] and Granger [64]. If the axial shrinkage strain is plotted against the moisture loss, the relationship has a S-shape with three smoothly connected sections. Initially, free water escapes the concrete without causing significant deformation. The amount of free water depends primarily on the curing conditions and can present a non-negligible fraction of the total moisture loss. Afterward, the moisture loss rate rapidly drops, and an approximately linear relationship with shrinkage can be established. In the last stage of drying, concrete still loses moisture, but without causing a significant shrinkage response.

In the present case, shown in Fig. 22, the mismatch between computed and measured shrinkage and moisture loss is obvious. The simulation results show an almost linear dependence of shrinkage on moisture loss, even though the sorption isotherm and the relationship between shrinkage and relative humidity are nonlinear. This is because at higher relative humidity (above 0.8), both the moisture capacity (slope of the moisture isotherm) and the shrinkage rate are higher and approximately proportional.

It should be noted that in Fig. 22 the experimental data come from different specimens (cylinder and prism with identical nominal thickness $D = 100$ mm) but prepared from identical concrete batch and same curing. In the experiment, significant weight loss continues despite negligible changes in shrinkage strain, whose evolution follows annual variations in ambient humidity. Obtaining this response with the current modeling approach is possible by simultaneously decreasing the parameter r_{sh} in (15) to emphasize the nonlinearity between shrinkage and relative humidity and by simultaneously increasing the parameter k_{sh} to obtain a correct value of the shrinkage strain. However, with this treatment, the response of the beams with one-sided exposure to ambient conditions becomes insufficiently sensitive to variations in humidity cycles.

4. Conclusions

This paper presents original data covering the first five years of an extensive experimental study on shrinkage, creep, and microcracking in drying concrete. In addition to conventional experiments, the study comprises a unique set of simply supported plain concrete beams with varying dimensions, with a span of up to 3 m, and different sealing configurations.

A data processing methodology has been developed to efficiently combine measurements from multiple locations on the beams and using different measuring techniques. An average curvature was selected as

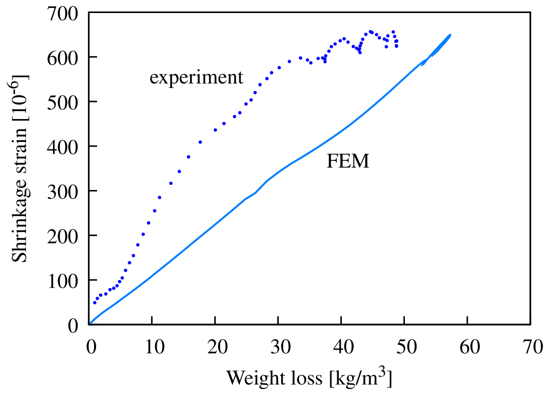

Fig. 22. Comparison of measured and computed relationship between moisture loss and axial shrinkage measured on specimens with identical nominal thickness D = 100 mm.

a representative quantity to characterize the behavior and its standard deviation to determine the variability and accuracy of different measurement techniques. In terms of both cost-efficiency and accuracy, the best approach to instrument such experiment seems to be the combination of two methods, namely DIC (inexpensive, measurement possible at multiple different locations to detect suspicious behavior such as localized cracking) and three automatic displacement sensors (two for axial shortening, one for vertical midspan deflection). In the present experiment, the accuracy of DIC was comparable to the demountable set of five digital indicators up to approximately 100 days, after which the error started to increase linearly.

Comparison of the experimental data with the results of the coupled hygro-mechanical finite element simulations has led to the following conclusions which are updating the optimistic findings in the preceding paper [5] covering the first year of the experiment.

(i) The predicted evolution of shrinkage-induced deflection of concrete beams subject to non-symmetric drying, obtained from a coupled simulation, was in good agreement with experimental observation in the first year of the experiment, as presented earlier in [5]. In that simulation, moisture transport was described with a Bažant-Najjar model, and the structural response was captured by a model based on the MPS theory. Subsequent measurements and simulation results started to substantially diverge. A significantly better, yet not perfect, response was obtained with the model for moisture transport by Künzel. This observation suggests that the generally accepted Bažant-Najjar model, also recommended by *fib*, might incorrectly predict the distribution of relative humidity across the thickness. This finding has paramount consequences, e.g., for predicting concrete durability associated with tensile cracking caused by restrained drying shrinkage.

(ii) The five-year data formed the foundation for improving the model based on the Microprestress-solidification theory, which has been found to overestimate creep under fluctuating ambient humidity. The constitutive model has been extended to mitigate excessive creep. However, the creep response remains spuriously sensitive to sampling and/or smoothing of the ambient relative humidity history.

(iii) The widely accepted dependence of the shrinkage rate on the relative humidity rate of pores via a constant shrinkage factor was generalized based on the earlier results of mesoscopic simulations and the experimental results on drying cement paste. With this improvement, the model was able to capture the evolution of the deflection of beams subjected to non-symmetric drying and annual humidity cycles.

The complete experimental data published in this paper and other supplementary materials are available online [65].

CRediT authorship contribution statement

Petr Havlásek: Writing – original draft, Visualization, Supervision, Methodology, Investigation, Formal analysis, Data curation, Conceptualization. **Vít Šmilauer:** Writing – review & editing, Data curation. **Václav Nežerka:** Writing – review & editing, Data curation.

Declaration of generative AI and AI-assisted technologies in the writing process

During the preparation of this work, the authors did not use any AI-based tools.

Declaration of competing interest

The authors have declared no conflict of interest

Acknowledgments

Financial support for this work was provided by the Czech Science Foundation (GA ČR), project number 22-35755K (SUMO: Sustainable design empowered by materials modeling, semantic interoperability, and multi-criteria optimization).

A special acknowledgment goes to P. Reiterman for providing data on the sorption isotherm.

Data availability

Complete dataset is available at Zenodo [65].

References

[1] Z. Bažant, M. Jirásek, Creep and Hygrothermal Effects in Concrete Structures, Springer Netherlands, 2018.
[2] A. Neville, Properties of Concrete, Wiley, 2011.
[3] Z.P. Bažant, L.J. Najjar, Nonlinear water diffusion in nonsaturated concrete, Mater. Struct. 5 (1972) 3–20.
[4] H. Künzel, Simultaneous Heat and Moisture Transport in Building Components, IRB, Stuttgart, 1995.
[5] P. Havlásek, V. Šmilauer, L. Dohnalová, R. Sovják, Shrinkage-induced deformations and creep of structural concrete: 1-year measurements and numerical prediction, Cem. Concr. Res. 144 (2021) 106402.
[6] P. Havlásek, M. Jirásek, Multiscale modeling of drying shrinkage and creep of concrete, Cem. Concr. Res. 85 (2016) 55–74.
[7] Z. Bažant, Mathematical models for creep and shrinkage of concrete, in: Z.P. Bažant, F.H. Wittmann (Eds.), Creep and Shrinkage in Concrete Structures, Wiley, 1982.
[8] C.M. Neubauer, T.B. Bergstrom, K. Sujata, Y. Xi, E.J. Garboczi, H.M. Jennings, Drying shrinkage of cement paste as measured in an environmental scanning electron microscope and comparison with microstructural models, J. Mater. Sci. 32 (1997) 6415–6427.
[9] Keeton, Study of Creep in Concrete, Phase 1 (I-Beam), U. S. Naval Civil Engineering Laboratory, Port Hueneme, California, 1965.
[10] E. Wallo, R. Yuan, J. Lott, C. Kesler, Prediction of Creep in Structural Concrete from Short Time Test, Progress Report 6, Department of Theoretical and Applied Mechanics. College of Engineering. University of Illinois at Urbana-Champaign, 1965.
[11] A.H. Bryant, C. Vadhanavikkit, Creep, shrinkage-size, and age at loading effects, ACI Mater. J. 84 (1987) 117–123.
[12] R. L'Hermite, M. Mamillan, Retrait et fluage des betons, Ann. ITBTP (Supplement 21) (1968) 1101–1120.
[13] T. Hansen, A. Mattock, Influence of size and shape of member on the shrinkage and creep of concrete, J. Am. Concr. Inst. 62 (2) (1966) 267–290.
[14] L. Dohnalová, P. Havlásek, Size effect on the ultimate drying shrinakge of concrete - experimental evidence and engineering practice, Acta Polytech. CTU Proc. 26 (2020) 13–18.
[15] V. Šmilauer, L. Dohnalová, M. Jirásek, J. Sanahuja, R. Wan-Wendner, Z. Bažant, Creep and Shrinkage Database of Laboratory Data, Tech. Rep., 2023.
[16] W.-C. Liao, J.-C. Chern, H.-C. Huang, T.-K. Liu, W.-Y. Chin, Establishment of analysis system and fast-access cloud-based database of concrete deformation, Comput. Concr. 28 (2021) 441–450.

[17] ISO 1920-8:2009, Testing of Concrete — Part 8: Determination of Drying Shrinkage of Concrete for Samples Prepared in the Field Or in the Laboratory, Standard, ISO, Switzerland, 2009.
[18] ISO 1920-9:2009, Testing of Concrete — Part 9: Determination of Creep of Concrete Cylinders in Compression, Standard, ISO, Switzerland, 2009.
[19] BS EN 12390-16:2019, Testing Hardened Concrete. Determination of the Shrinkage of Concrete, Standard, European committee for standardization, Brussels, 2019.
[20] BS EN 12390-17:2019, Determination of Creep of Concrete in Compression, Standard, European committee for standardization, Brussels, 2019.
[21] Standard Test Method for Length Change of Hardened Hydraulic-Cement Mortar and Concrete, Standard, ASTM International, West Conshohocken, PA, 2017.
[22] Standard Test Method for Creep of Concrete in Compression, Standard, ASTM International, West Conshohocken, PA, 2015.
[23] O. Coussy, Poromechanics, John Wiley & Sons, Ltd, 2004.
[24] A. Aili, M. Vandamme, J.-M. Torrenti, B. Masson, A viscoelastic poromechanical model for shrinkage and creep of concrete, Cem. Concr. Res. 129 (2020) 105970.
[25] P. Yu, Y. Duan, Q. Fan, S. Tang, Improved MPS model for concrete creep under variable humidity and temperature, Constr. Build. Mater. 243 (2020) 118183.
[26] S. Rahimi-Aghdam, Z.P. Bažant, G. Cusatis, Extended microprestress-solidification theory for long-term creep with diffusion size effect in concrete at variable environment, J. Eng. Mech. 145 (2) (2019) 04018131.
[27] G. Di Luzio, G. Cusatis, Solidification–microprestress–microplane (SMM) theory for concrete at early age: Theory, validation and application, Int. J. Solids Struct. 50 (6) (2013) 957–975.
[28] V. Gribniak, Shrinkage Influence on Tension-Stiffening of Concrete Structures (Ph.D. thesis), 2009.
[29] D. Branson, B. Meyers, K. Kripanarayanan, Time-dependent deformation of non-composite and composite prestressed concrete structures, Symp. Concr. Deform. (1970) 15–43.
[30] B. Patzák, OOFEM home page, 2000, http://www.oofem.org.
[31] B. Patzák, OOFEM - an object-oriented simulation tool for advanced modeling of materials and structures, Acta Polytech. 52 (6) (2012) 59–66.
[32] Z. Bažant, P. Havlásek, M. Jirásek, Microprestress-solidification theory: Modeling of size effect on drying creep, in: N. Bicanic, H. Mang, G. Meschke, R. de Borst (Eds.), Computational Modelling of Concrete Structures, CRC Press/Balkema, EH Leiden, The Netherlands, 2014, pp. 749–758.
[33] P. Havlásek, Creep and Shrinkage of Concrete Subjected to Variable Environmental Conditions (Ph.D. thesis), Czech Technical University in Prague, 2014.
[34] R. de Borst, J.J.C. Remmers, A. Needleman, M.-A. Abellan, Discrete vs smeared crack models for concrete fracture: bridging the gap, Int. J. Numer. Anal. Methods Geomech. 28 (7–8) (2004) 583–607.
[35] Z.P. Bažant, B.H. Oh, Crack band theory for fracture of concrete, Matér. Constr. 16 (1983) 155–177.
[36] Fédération Internationale du Béton, Model Code 2010, No. vol. 65 in fib Bulletin, International Federation for Structural Concrete (fib), 2012.
[37] Z. Bažant, S. Baweja, Creep and shrinkage prediction model for analysis and design of concrete structures: Model B3, in: Adam Neville Symposium: Creep and Shrinkage - Structural Design Effects, 2000.
[38] BS EN 12390-13:2013: Testing Hardened Concrete Part 13: Determination of Secant Modulus of Elasticity in Compression, BSI British Standards Publication, 2013.
[39] BS EN 12390-3:2009: Testing Hardened Concrete Part 3: Compressive Strength of Test Specimens, BSI British Standards Publication, 2011.
[40] V. Nežerka, P. Havlásek, A lightweight DFT-based approach to the optical measurement of displacements using an open-source Python code, Exp. Tech. (2022).
[41] M. Van Genuchten, A closed-form equation for predicting the hydraulic conductivity of unsaturated soils, Soil Sci. Am. J. 44 (1980).
[42] Z.P. Bažant, A.P. Hauggaard, S. Baweja, F.J. Ulm, Microprestress solidification theory for concrete creep. I: Aging and drying effects, J. Eng. Mech. 123 (1997) 1188–1194.
[43] M. Jirásek, P. Havlásek, Microprestress-solidification theory of concrete creep: Reformulation and improvement, Cem. Concr. Res. 60 (2014) 51–62.
[44] F. Wittmann, Kriechverformung des Betons unter statischer und unter dynamischer Belastung, Rheol. Acta 10 (1971).
[45] H. Fahmi, M. Polivka, B. Bresler, Effects of sustained and cyclic elevated temperature on creep of concrete, Cem. Concr. Res. 2 (1972) 591–606.
[46] G. Pickett, The effect of change in moisture-content on the creep of concrete under a sustained load, J. Am. Concr. Inst. 38 (1942) 333–355.
[47] I. Maruyama, H. Sasano, M. Lin, Impact of aggregate properties on the development of shrinkage-induced cracking in concrete under restraint conditions, Cem. Concr. Res. 85 (2016) 82–101.
[48] J. Bisschop, Drying Shrinkage Microcracking in Cement-Based Materials, DUP Science, 2002.
[49] A. Idiart, J. Bisschop, A. Caballero, P. Lura, A numerical and experimental study of aggregate-induced shrinkage cracking in cementitious composites, Cem. Concr. Res. 42 (2) (2012) 272–281.
[50] V. Baroghel-Bouny, M. Mainguy, T. Lassabatere, O. Coussy, Characterization and identification of equilibrium and transfer moisture properties for ordinary and high-performance cementitious materials, Cem. Concr. Res. 29 (1999) 1225–1238.
[51] H. Jennings, Colloid model of C–S–H and implications to the problem of creep and shrinkage, Mater. Struct. 37 (2004) 59–70.
[52] I. Maruyama, Y. Nishioka, G. Igarashi, K. Matsui, Microstructural and bulk property changes in hardened cement paste during the first drying process, Cem. Concr. Res. 58 (2014) 20–34.
[53] T. Rougelot, F. Skoczylas, N. Burlion, Water desorption and shrinkage in mortars and cement pastes: Experimental study and poromechanical model, Cem. Concr. Res. 39 (1) (2009) 36–44.
[54] A.E. Idiart, C.M. López, I. Carol, Modeling of drying shrinkage of concrete specimens at the meso-level, Mater. Struct. 44 (2011) 415–435.
[55] P. Grassl, H. Wong, N. Buenfeld, Influence of aggregate size and volume fraction on shrinkage induced micro-cracking of concrete and mortar, Cem. Concr. Res. 40 (2010) 85–93.
[56] I. Maruyama, H. Sasano, Strain and crack distribution in concrete during drying, Mater. Struct. 47 (2014) 517–532.
[57] A. Hilaire, F. Bendoudjema, A. Darquennes, Y. Berthaud, G. Nahas, Modeling basic creep in concrete at early-age under compressive and tensile loading, Nucl. Eng. Des. 269 (2014) 222–230.
[58] J. Tailhan, C. Boulay, P. Rossi, F. Le Maou, E. Martin, Compressive, tensile and bending basic creep behaviours related to the same concrete, Struct. Concr. 14 (2) (2013) 124–130.
[59] N. Ranaivomanana, S. Multon, A. Turatsinze, Basic creep of concrete under compression, tension and bending, Constr. Build. Mater. 38 (2013) 173–180.
[60] N. Ranaivomanana, S. Multon, A. Turatsinze, Tensile, compressive and flexural basic creep of concrete at different stress levels, Cem. Concr. Res. 52 (2013) 1–10.
[61] P. Rossi, J. Tailhan, F. Le Maou, Comparison of concrete creep in tension and in compression: Influence of concrete age at loading and drying conditions, Cem. Concr. Res. 51 (2013) 78–84.
[62] H. Jennings, J. Bullard, J. Thomas, J. Andrade, J. Chen, G. Scherer, Characterization and modeling of pores and surfaces in cement paste: Correlations to processing and properties, J. Adv. Concr. Technol. 6 (2008) 1–25.
[63] C. Aguilar, Estudio del Comportamiento y Desarrollo de una Metodologia de Prediccion de la Retraccion Hidraulica de Hormigones (Ph.D. thesis), Pontificia Universidad Catolica de Chile. Escuela de Ingenieria, 2005, (in Spanish).
[64] L. Granger, Comportement Differe du Beton Dans les Enceintes de Centrales Nucleaires: Analyse et Modelisation (Ph.D. thesis), LCPC, Paris, France, 1995, (in French).
[65] P. Havlásek, V. Šmilauer, V. Nežerka, Data for: Drying-induced deformation in concrete: Insights from a 5-year study. http://dx.doi.org/10.5281/zenodo.13843475.